Chemical Science

ROYAL SOCIETY OF CHEMISTRY

EDGE ARTICLE

View Article Online
View Journal



Cite this: DOI: 10.1039/d5sc08815a

All publication charges for this article have been paid for by the Royal Society of Chemistry

# Hydro-photo-synergy unlocks deep and reversible chemistry of solid-state lithium–oxygen batteries

Sijia Chi,[abc] Zhenshen Li,[abc] Xunjie Yin,[abc] Shuoyi Chen,[abc] Xuerui Yi,[abc] Yiqiao Wang,[abc] Yong Guo,[abc] Fangbing Li,[ab] Shichao Wu *[abc] and Quan-Hong Yang *[abcd]

Received 12th November 2025
Accepted 19th December 2025

DOI: 10.1039/d5sc08815a

rsc.li/chemical-science

Harnessing light to drive high-energy batteries is an intriguing goal, yet photoactivity often fails for reasons that have remained elusive, which is starkly exemplified in photo-assisted solid-state lithium–oxygen batteries. Here, we identify photo-shielding by opaque, ionically resistive discharge products as the critical, previously overlooked failure mechanism. This "catalyst blinding" effect not only blocks light but also passivates the electrochemical interface, causing a catastrophic kinetic shutdown. We overcome this limitation with a "hydro-photo-synergy" strategy, using controlled water vapor to shift the solid-state electrochemistry from a $2e^-$ to an efficient $4e^-$ pathway and transform the product into highly transparent, ionically conductive products. This dual optical and electrochemical enhancement sustains photocatalysis for deep and reversible reactions, unlocking a 2-fold increase in accessible capacity, a low overpotential (0.3 V), and outstanding stability (>170 cycles for 34 mA h $cm^{-2}$). This work establishes *in situ* product engineering as a new paradigm to unlock high-energy solid-state photo-electrochemical devices.



## 1. Introduction

Solid-state photo-chemical systems, encompassing diverse applications such as photocatalytic $CO_2$ reduction, photocatalytic $N_2$ fixation, and photolithography, represent a frontier in sustainable energy and advanced manufacturing.[1–3] A unifying theme in these technologies is the precise use of light to drive chemical transformations at solid interfaces. Leveraging this principle in high-energy storage, specifically by applying photo-assistance to high-energy-density solid-state lithium–oxygen batteries (SSLOBs),[4–9] offers a compelling strategy to overcome their sluggish oxygen reduction and evolution reaction (ORR/OER) kinetics and perhaps even bypass thermodynamic limitations.[10–13] While various photocatalysts (*e.g.*, $C_3N_4$,[14,15] $TiO_2$–$Fe_2O_3$,[16] Au/rGO,[17] single-atom catalysts (SACs),[18] p-$MoS_2$ (ref. 19)) have been increasingly explored, reported photo-assisted Li–$O_2$ batteries universally exhibit severely limited discharge capacities (<5000 mAh $g^{-1}$)[15,16,20,21] and ultralow cycling cut-off capacities (<0.1 mAh $cm^{-2}$),[20–24] leaving the true potential of this approach unrealized and its fundamental limitations poorly understood.

Photo-assistance offers a powerful tool to control Li–$O_2$ reaction pathways.[25,26] During discharge, the photo-excited catalyst generates electron-hole pairs, with the electrons facilitating the ORR.[15,27] In liquid systems, the photo-field can enhance the adsorption of the lithium superoxide ($LiO_2$) intermediate, inhibiting its dissolution and thereby favoring a two-electron pathway to form $Li_2O_2$ thin films.[24,28,29] Higher current densities or illumination intensities were found to further encourage the formation of these $Li_2O_2$ thin films.[17] However, the expected benefits are often counteracted because the absence of a liquid medium for ion transport severely restricts $Li_2O_2$ growth within the solid-state cathode, regardless of the initial growth morphology, leading to premature passivation and capacity limitations.[30,31] Furthermore, the subsequent charging process in photo-assisted SSLOBs (P-SSLOBs) is frequently challenged by high overpotentials and the incomplete decomposition of the $Li_2O_2$ product. Despite the observation on morphology control issue, a deeper mechanistic understanding of the interplay between photo-effects, solid-state capacity limitations and reaction kinetics is lacking.

Here we identify photo-shielding as the critical, previously overlooked bottleneck suppressing the performance of P-SSLOBs by photo-shielding from the opaque $Li_2O_2$ discharge product. This "catalyst blinding" effect causes a sharp potential slump and negates the benefits of photo-assistance (Fig. 1b). We

[a]*Nanoyang Group, Tianjin Key Laboratory of Advanced Carbon and Electrochemical Energy Storage, School of Chemical Engineering and Technology, National Industry-Education Integration Platform of Energy Storage, and Collaborative Innovation Centre of Chemical Science and Engineering, Tianjin University, Tianjin 300072, China. E-mail: wushichao@tju.edu.cn; qhyangcn@tju.edu.cn*

[b]*State Key Laboratory of Chemical Engineering and Low-Carbon Technology, Tianjin University, Tianjin 300072, China*

[c]*Haihe Laboratory of Sustainable Chemical Transformations, Tianjin, 300192, China*

[d]*Joint School of National University of Singapore and Tianjin University, International Campus of Tianjin University, Binhai New City, Fuzhou 350207, China*

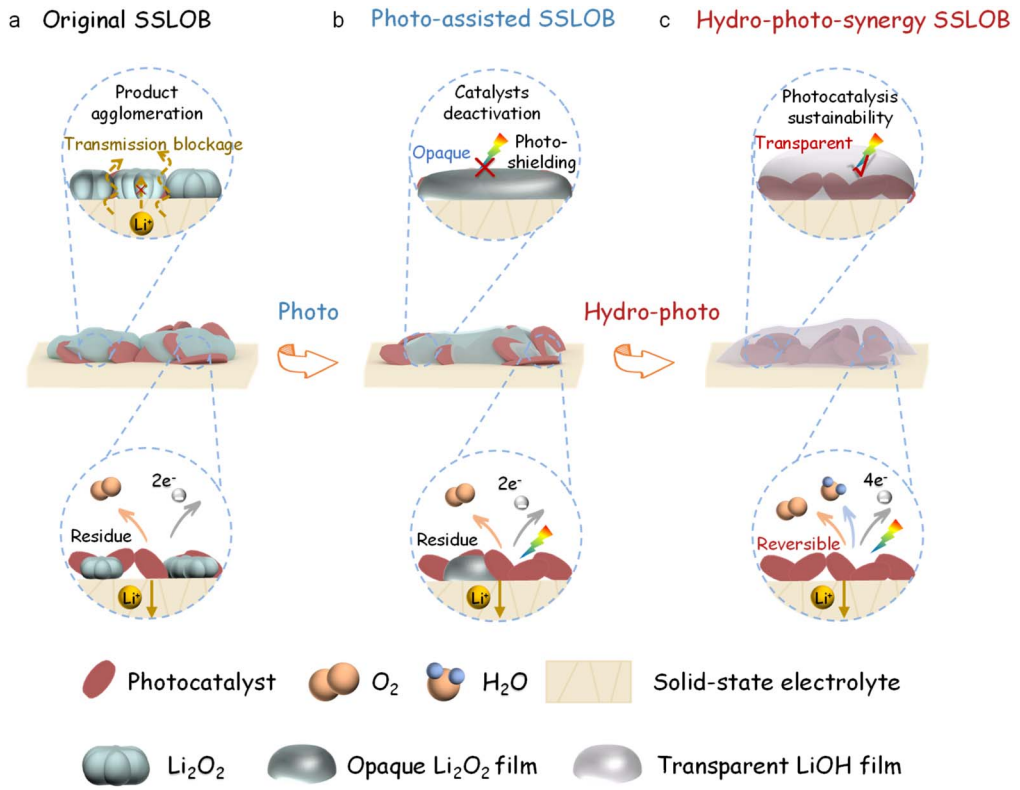


Fig. 1 Photo-shielding failure mechanism in P-SSLOBs and our proposed hydro-photo-synergy solution. (a) In conventional dark conditions, the $Li_2O_2$-based $2e^-$ reaction leads to product agglomeration. (b) Under photo-assistance, the same reaction produces an opaque $Li_2O_2$ film that "blinds" and deactivates the photocatalyst, causing premature failure. (c) The hydro-photo-synergy strategy introduces controlled water vapor, redirecting the reaction to a $4e^-$ pathway that forms highly transparent LiOH. Our strategy prevents photo-shielding by transforming the opaque discharge product ($Li_2O_2$) into a transparent one (LiOH), ensuring sustained photocatalysis.

overcome this by introducing a hydro-photo-synergy strategy: controlled water vapor induces an *in situ* transformation of opaque $Li_2O_2$ to transparent LiOH (Fig. 1c). This pivotal conversion not only sustains photocatalysis by eliminating light blockage but also fundamentally redirects the electrochemistry. The system shifts from a passivating 2-electron pathway to a highly efficient 4-electron pathway that forms LiOH, a product also more amenable to rapid charge transport. This combined optical and electrochemical enhancement boosts oxygen utilization, suppresses side reactions, and drastically reduces recharging overpotentials. Our strategy yields P-SSLOBs with a discharge capacity of 7 mAh $cm^{-2}$, a charge overpotential of only ~0.3 V, and stability exceeding 170 cycles for 34 mAh $cm^{-2}$.

## 2. Experimental section

### 2.1 Synthesis of (110) $Fe_2O_3$

2.76 g $FeCl_3 \cdot 6H_2O$ (Aladdin, 99%) and 5.25 g $CH_3COONa \cdot 3H_2O$ (Aladdin, 99%) were dissolved in 35 mL anhydrous ethanol and stirred vigorously for 10 minutes. The solution was transferred into a 50 mL Teflon-lined stainless-teel autoclave and heated in an oven at 200 °C for 24 h. After being cooled down, the resulting powder was vacuum-filtrated and then dried at 80 °C.

### 2.2 Synthesis of $Li_{1.3}Al_{0.3}Ti_{1.7}(PO_4)_3$ pellet

$Li_{1.3}Al_{0.3}Ti_{1.7}(PO_4)_3$ (LATP) raw powder was purchased from GanfengLiEnergy. 0.40 g of the LATP powder was uniaxially pressed into a green pellet for 5 min at 800 MPa using a 12 mm stainless-steel mold. The pellets were covered with the same powder and sintered at 900 °C for 6 hours at a heating rate of 2 °C $min^{-1}$ in MgO crucibles. The pellets were reduced to a thickness of 850 μm with 240-grit SiC sandpaper, followed by polishing with 2000, 4000 and 8000-grit metallographic sandpapers.

### 2.3 Preparation of the polymer electrolyte

PEO ($M_W$ = 600 000, Sigma) and LiTFSI (Aladdin) were firstly dissolved in acetonitrile (Macklin), and stirred for 12 hours to form a uniform solution with an EO/Li molar ratio of 14 : 1. Subsequently, the solution was cast into a polytetrafluoroethylene (PTFE) dish with a thickness of 6 μm. PEO membranes were finally dried for 48 hours.

### 2.4 Preparation of the cathode

MWCNTs (XFNANO), LATP nanoparticles and (110) $Fe_2O_3$ with a weight ratio of 1 : 1:6 was high-energy ball milled at a rate of 500 rpm for 15 h, and then dispersed into solution composed of 5% polyvinylidene fluoride and 95% *N*-methyl-2-pyrrolidone.

The solution was uniformly painted on one side of LATP pellet and heated at 500 °C for 60 min in Ar atmosphere. The mass of the air electrode was about 0.5 mg.

### 2.5 Battery assembly and test

A pouch-type Li metal anode was fabricated to protect the Li metal from moisture during operation in the humid atmosphere. The cathode/LATP plate, PEO, and a piece of Li foil (12 mm in diameter and 0.5 mm in thickness) were vacuum-sealed using thermoplastic sealing film (Meltonix 1170-25, Solaronix) while leaving a 5-mm-diameter window. Then thus assembled Li–$O_2$ cell was operated in a PTFE chamber with a vial containing a small amount of water; before this step, purging was performed using pure $O_2$. For photo-assisted charge, the Xe lamp (CEAULIGHT-HXF300) was opened at the current of 15 A to irradiate the cell through the vessel. The assembled cell was tested on a battery tester (LAND CT2001A) between 2.0 and 4.2 V and electrochemical impedance spectra (EIS) were tested on a CHI660E electrochemical workstation (Shanghai, China).

### 2.6 Material characterization

X-Ray diffraction (XRD, Rigaku MiniFlex-600) patterns were recorded to confirm the successful synthesis of (110) $Fe_2O_3$. Fourier transform infrared (FTIR) spectra were recorded on a Thermo Scientific Nicolet iS50 spectrometer to test the information of functional groups. Raman spectra were recorded on a Raman spectrometer (HORIBA Jobin Yvon, LabRAM HR Evolution, Japan) with an Ar ion laser of $\lambda = 785$ nm. The scanning electron microscope (SEM, S4800) was employed to determine the morphologies of the surface and cross-section of all samples. X-ray photoelectron spectroscopy (XPS, Thermo Fisher Scientific ESCALAB Xi$^+$, Al K$\alpha$ radiation, $h_\nu = 1486.6$ eV, UK) was used to determine surface chemical composition. Gas production was recorded by differential electrochemical mass spectrometry (DEMS, Linglu Instruments, Shanghai).

## 3. Results and discussion

### 3.1 Identifying photo-shielding and the hydro-photo synergy breakthrough

In a conventional environment, the P-SSLOB exhibits a characteristic performance failure that severely limits its practical capacity. To unveil this limitation, we investigated the discharge behavior of a (110) $Fe_2O_3$-based cathode under photo (Fig. S1).[28] As shown in Fig. 2a, under an illumination of 40 W, the battery initially discharges at a high-potential plateau of 2.8 V. However, upon reaching a mere areal capacity of 0.7 mAh cm$^{-2}$, the battery undergoes a sharp potential slump to ~2.4 V (Fig. 2a). This lower voltage is consistent with that observed under dark conditions.

To diagnose the root cause, we examined the influence of light intensity. Increasing the light intensity to 45 W delays the potential slump to occur at a later stage, with the high-potential capacity contributing 51.8% of the total (Fig. 2b and c). Raising the light intensity further to 50 W delays the slump even more, increasing the contribution of the high-potential capacity to 67.8% (Fig. 2b and c). Nevertheless, the ultimate failure could not be prevented. This behavior indicates that while a higher photon flux can temporarily compensate for performance loss, the fundamental issue lies in a progressive light attenuation at the buried catalytic interface as the discharge product accumulates.

This phenomenon can be quantitatively described within the Beer–Lambert law framework, which models the local light intensity, $I(z)$, reaching a catalytic site at a depth $z$ beneath the product layer:

$$I(z) = I_0 e^{-k_{opt} d} \quad (1)$$

Here $I_0$ denotes the incident light intensity and $k_{opt}$ is the optical attenuation coefficient. This model reveals two primary mitigation strategies: (i) increasing the incident intensity $I_0$, or, more fundamentally, (ii) decreasing the effective optical attenuation coefficient $k_{opt}$ of the product itself. Our experimental results have already shown the inherent limitations of the first strategy; it offers only temporary and partial improvements constrained by practical illumination limits.

Therefore, we focused on the second, more intrinsic strategy: engineering the physicochemical properties of the discharge product to reduce its optical attenuation coefficient $k_{opt}$, *i.e.*, improving the optical transparency, providing a more intrinsic and sustainable pathway to enhance light penetration. By tailoring the physicochemical properties of the discharge products or engineering the electrode–electrolyte interface, light absorption within the growing product layer can be fundamentally suppressed.

To alter the reaction products, we implemented a hydro-photo-synergy strategy by introducing water vapor. As shown in Fig. S5, although the two-plateau phenomenon still occurred under intensities of 40 W and 45 W, the proportions of high-potential plateau capacity reached 36.6% and 76.5%, respectively (Fig. 2c)—both higher than those under photo at the same intensities (25.4% and 51.8%) (Fig. 2c). As shown in Fig. 2b, strikingly, at an intensity of 50 W, the potential slump was completely eliminated, with the potential plateau accounting for 100% of the total discharge. This indicates that our strategy fully inhibits the photo shielding effect and maintains catalyst activity throughout a deep discharge. This unlocked a significant increase in discharge capacity, reaching 7 mAh cm$^{-2}$ in the hydro-photo-synergistic cell in stark contrast to the premature failure of the cell under photo (3.63 mAh cm$^{-2}$) (Fig. 2b). For a direct comparison of the hydro-photo strategy, the ratios of high/low-potential capacities and the unused capacity ratio relative to the maximum capacity (7 mAh cm$^{-2}$) are plotted in Fig. 2c. The "Unused Capacity" is calculated using the formula: unused capacity (%) = [(7.04 – measured capacity)/7.04] × 100%. As defined by the axes, the ideal state corresponds to an "Unused Capacity" of 0, a "Low-potential Capacity" of 0, and a "high-potential capacity" of 1, meaning that the region with optimal performance is located in the upper-left quadrant of the phase diagram. The results show that the data points under the hydro-photo strategy are predominantly distributed in this

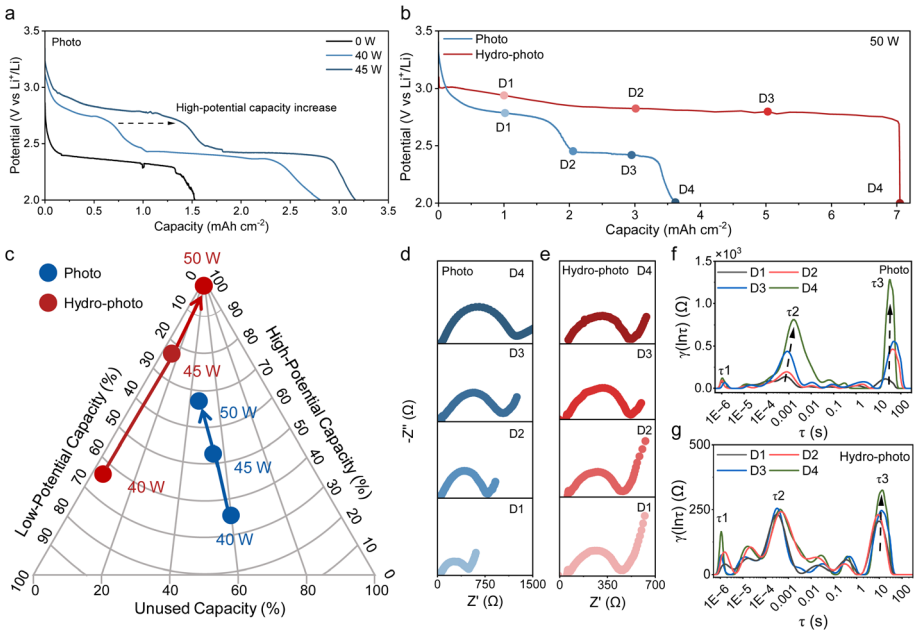


Fig. 2 Discharge depth enhancements resulting from the hydro-photo-synergy strategy. (a) Discharge voltage profiles show the sharp potential slump at intensity of 40 W and alleviate at 45 W under photo. (b) Discharge voltage profiles show the elimination of the sharp potential slump and a significant capacity increase under hydro-photo compared to photo at a current density of 0.1 mA cm$^{-2}$ at 50 W. (c) The contribution of the high-potential photocatalytic plateau is increased under hydro-photo system across different light intensities. (d and e) *In situ* electrochemical impedance spectroscopy (EIS) tracks the kinetic evolution during discharge, comparing (d) the rapid impedance rise (passivation) under photo with (e) the sustained low impedance (fast kinetics) under hydro-photo. (f and g) DRT calculated from EIS measurements at different discharge states under (f) photo and (g) hydro-photo. Hydro-photo-synergy strategy overcomes premature failure by maintaining rapid kinetics and preventing catastrophic electrode passivation.

region, indicating its favorable capacity performance. In contrast, the data points obtained under photo conditions are mainly concentrated in the lower-right quadrant, reflecting comparatively inferior performance.

The hydro-photo-synergistic cell shows a fundamental improvement of the reaction kinetics, as revealed by *in situ* electrochemical impedance spectroscopy (EIS) conducted throughout the discharge process (Fig. 2d and e). Both the conventional and hydro-photo-synergistic systems began with a comparable initial cell resistance of approximately 500 Ω. However, their kinetic behavior diverged sharply as discharge progressed. In system under photo, the impedance rapidly doubled as the cell reached its low-potential plateau, signaling a catastrophic loss of kinetic activity (Fig. 2d). This impedance surge is indicative of severe electrode passivation and a shut-down of charge transfer processes. In stark contrast, the cell operating under our hydro-photo-synergy strategy maintained a consistently low and stable impedance throughout its entire high-capacity discharge (Fig. 2e).

According to the further analysis of distribution of relaxation time (DRT), three dominant peaks are observed (Fig. 5f and g), labeled as τ1, τ2 and τ3, respectively. τ1 ($\tau \approx 10^{-6}$ s) is related to the RGB (grain boundary impedance) of solid-state electrolytes.[32,33] $\tau_2$ ($1 \times 10^{-4}$–$1 \times 10^{-3}$ s) is attributed to ion transport.[34] Since the charge transfer process has a longer relaxation time and shorter characteristic frequency than the ion mass transfer process, the τ3 peak is related to the charge transfer process of the cathode.[35] The change of τ3 peak is related to the product state of the cathode. As the discharge proceeds, the product gradually forms on the surface of the cathode, hindering the transfer of electrons, and thus charge transfer impedance ($R_{ct}$) of both batteries shows a steady growth. The comparison of the evolution laws of the SSLOB under the two conditions revealed that during the discharge process, the $R_{ct}$ under hydro-photo-synergy remained consistently lower than that under photo, with a slower rate of increase. Even at the end of discharge, it was only 330 Ω, significantly lower than the 1200 Ω observed under photo. This indicates that the product formed under hydro-photo-synergy effectively facilitate charge transfer during the reaction. Similar to the trend observed with the τ3 peak, the intensity of the τ2 peak (corresponds to ionic mass transfer resistance) continued to increase under photo, while no significant change was observed under hydro-photo-synergy. This demonstrates that the variation in ionic mass transfer resistance is also closely related to the state of the products. This sustained low impedance provides direct evidence of rapid and stable reaction kinetics, which is the underlying reason for the cell's ability to operate at a high potential and achieve a deep discharge. The dramatic difference in kinetic behavior strongly suggests that our strategy fundamentally alters the nature of the discharge process and the properties of the resulting product on the electrode surface.

### 3.2 Product transformation and transparency engineering

To understand the origin of the dramatically different kinetic behaviors observed under the two conditions, we investigated the composition and physical properties of the respective discharge products. The composition and morphology of the discharge products on the cathode were investigated by Raman, Fourier Transform infrared spectroscopy (FTIR), X-ray Photoelectron Spectroscopy (XPS) and Scanning Electron Microscope (SEM). The Raman spectra of discharge products under photo in Fig. 3a shows a characteristic peak at 789 $cm^{-1}$ corresponding to $Li_2O_2$ while the spectra of discharge products under hydro-photo shows a characteristic peak at ~3660 $cm^{-1}$ corresponding to LiOH, which indicates that the discharge product of P-SSLOB is $Li_2O_2$ under photo and is LiOH under hydro-photo. The results were similarly verified by FTIR (Fig. 3b) and XPS spectra (Fig. 3c and d). The SEM images (Fig. 3e and f) show that the discharge products under both conditions were membranous, but the product formed under hydro-photo was more transparent in comparison. This evidence points to a clear mechanism proposed in eqn (1): the accumulation of opaque $Li_2O_2$ physically blocks light from reaching the photocatalyst, causing the observed deactivation and potential slump—a severe photo-shielding effect.

We measured and compared the transparency of $Li_2O_2$ and LiOH by a custom photoresistor setup (Fig. 3g) with a photoresistor, while using a glass sheet as a blank sample. The pressed pellet is placed in front of the photoresist and the resistance ($R$) obtained by shining a flashlight through the

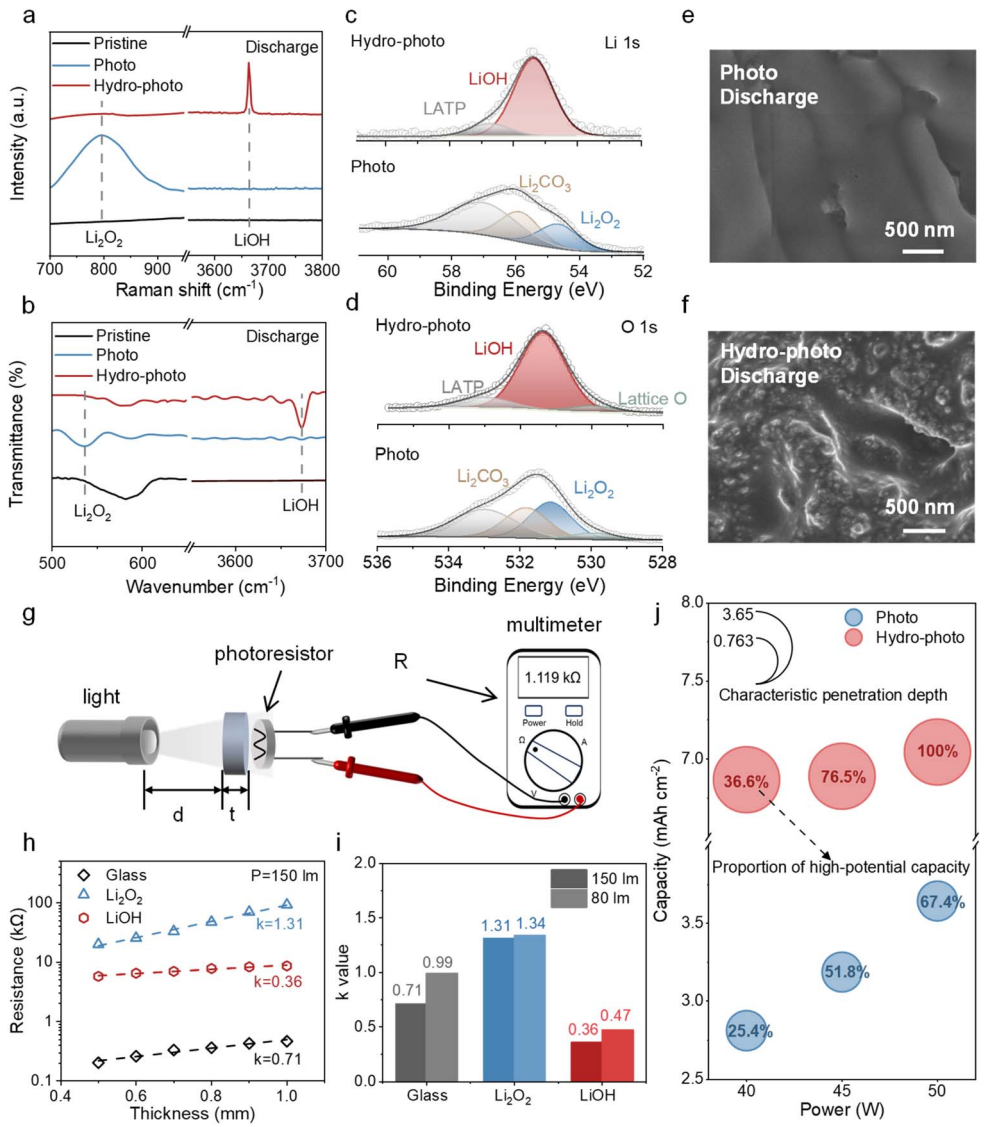


Fig. 3 Discharge product transformation and links it to enhanced optical transparency. (a–d) Spectroscopic analyses including (a) Raman, (b) FTIR, and (c and d) XPS confirm the discharge product is $Li_2O_2$ under photo and transforms to LiOH under hydro-photo. (e and f) SEM images visually compare the morphology of the products. (g) A schematic illustrates the custom-built setup for measuring optical transparency. (h and i) Transparency tests reveal that LiOH (small $k$-value) is significantly more transparent than $Li_2O_2$ (large $k$-value), with its transparency being less affected by thickness. (j) A direct correlation is shown between the product's light transmittance ($T$) and the cell's achievable discharge capacity. *In situ* formation of highly transparent LiOH is the direct cause for mitigating photo-shielding and unlocking high discharge capacity.

pellet is related to its transparency. The stronger the light shining on the photoresistor, the smaller its resistance. The results of the transparent tests are shown in Table S1. The results revealed that light passing through a $Li_2O_2$ pellet resulted in a resistance approximately five times higher than through a LiOH pellet of similar thickness, confirming the low intrinsic transparency of $Li_2O_2$ (Fig. 3h, i). In order to show the difference in transparency between the two more intuitively, we processed the values obtained from the tests and plotted them. We first quantified the transparency as the characteristic penetration depth ($D$). Based on the Beer–Lambert law and the power-law response of the photoresistor ($R \propto I^{-\gamma}$), we derived the linear relationship

$$\ln R \propto k \times d \tag{2}$$

The penetration depth is defined as the reciprocal of the effective attenuation coefficient ($k$), *i.e.*,

$$D = 1/k \tag{3}$$

The calculations yielded $D_{Li_2O_2} = 0.763$ and $D_{LiOH} = 2.778$. Subsequently, we employed a Langmuir saturation model to describe the dependence of $Q$ on $D$:

$$Q = (Q_{max} \times D)/(K + D) \tag{4}$$

By substituting the experimental data points, we determined the theoretical capacity limit ($Q_{max} = 10.87$ mAh) and the half-saturation constant ($K = 1.51$). Consequently, the quantitative relationship between $Q$ and $D$ is expressed as $Q = 10.87D/(1.51 + D)$ , as illustrated in Fig. S8.

The profile exhibits two mechanically distinct zones. $Li_2O_2$ falls within the rapid growth region, where the capacity is highly sensitive to variations in optical depth ($D < K$). This implies that the discharge process is strictly rate-determined by light transmission efficiency. Conversely, LiOH lies in the asymptotic saturation region ($D > K$). In this regime, although the optical penetration depth increases drastically, the capacity growth plateaus as it converges towards the theoretical maximum. This saturation confirms a paradigm shift in the failure mechanism: the removal of the optical bottleneck allows the system to reach its physical limit, where capacity becomes constrained by the available electrode pore volume (spatial limitation) rather than photon supply.

The results after varying the illumination intensity are shown in Table S2, Fig. 3i, and S7, from which it can be observed that the resistance values through the three materials increase as the intensity decreases, suggesting that the intensity also has an effect on the photo-assisted system. The relationship between the characteristic penetration depth and the discharge capacity is consolidated and presented in Fig. 3j. Regardless of the illumination intensity, the higher the transmittance of the product, the higher the discharge capacity of the battery. The direct correlation between product transparency and discharge capacity underscores the critical role of this physical property. This demonstrates that LiOH enabled by the hydro-photo-synergy strategy can effectively suppress the photo-shielding phenomenon throughout deposition. Moreover, to provide a standardized and quantitative comparison of optical transparency, we performed UV-visible transmittance measurements on LiOH and $Li_2O_2$ pellets. As shown in Fig. S10, LiOH exhibits consistently higher transmittance than $Li_2O_2$ across the wavelength range of 300–500 nm. This result further confirms the superior optical transparency of LiOH and substantiates its role in mitigating photo-shielding, consistent with our earlier photoresistor-based measurements.

### 3.3 Shifting to a four-electron pathway

The introduction of water does more than just alter product transparency; it fundamentally redirects the electrochemical reaction pathway. We first observed a high equilibrium potential under hydro-photo (~3.2 V) compared to photo (2.96 V) *via* galvanostatic intermittent titration technique (GITT) tests, indicating a thermodynamic shift to a different reaction (Fig. 4a and b). To provide direct evidence for this pathway change, we performed *in situ* differential electrochemical mass spectrometry (DEMS). The ratio of electrons transferred to oxygen consumed ($e^-/O_2$) during discharge was calculated to be 1.99 : 1 ($4.48 \times 10^{-5}$ mol and $2.25 \times 10^{-5}$ mol) under photo, confirming the expected 2-electron reaction to form $Li_2O_2$.[36–38] In stark contrast, the ratio under hydro-photo was 3.93 : 1 ($4.48 \times 10^{-5}$ mol and $1.1 \times 10^{-5}$ mol), unequivocally demonstrating a shift to a 4-electron electrochemical process to form LiOH (Fig. 4c).

Furthermore, this 4-electron pathway enhances reaction reversibility. During charging, the loss of oxygen ($O_2$ consumed *vs.* $O_2$ evolved) was substantially greater under photo, which we attribute to parasitic reactions where the aggressive $Li_2O_2$ product attacks the carbon cathode to form $Li_2CO_3$ (Fig. 4e).[30,39–41] The corresponding $CO_2$ release during charging under photo confirms this side reaction (Fig. S11). In contrast, the more stable LiOH product under hydro-photo mitigates these side reactions, leading to improved cycling efficiency.

To further elucidate the reaction mechanism at the molecular level, we directly detected the formation of the key intermediate lithium hydroperoxide (LiOOH) during the discharge process *via in situ* Raman spectroscopy (Fig. S13). Based on the experimental evidence, we propose the following reaction pathway: $O_2$ react with $Li^+$ and electrons to form the oxygen-containing intermediate LiOOH, which subsequently undergoes further reduction with $Li^+$ and electrons at the interface or active sites to yield LiOH. This result strongly supports the conclusion in the manuscript regarding the water-induced change in the reaction pathway.

In summary, we can get the different reaction paths of P-SSLOB under the two conditions. Photoelectrons generated by photoexcitation of the catalyst under photo react with oxygen in a ratio of 2 : 1 to form the less transmissive product $Li_2O_2$, which covers the catalyst surface leading to catalyst deactivation during the discharge process. However, under hydro-photo, photoelectrons and oxygen participate in the reaction at a ratio of 4 : 1, and LiOH with high transparency is formed directly without the process of generating $Li_2O_2$. Such a reaction

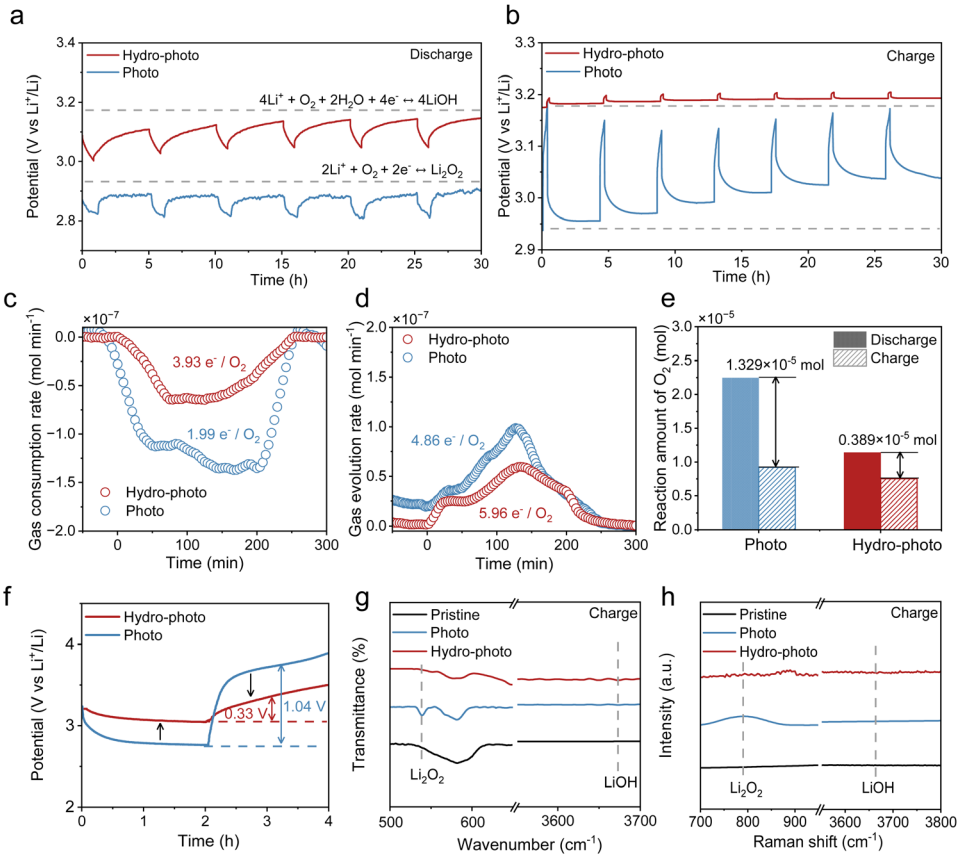


Fig. 4 Electrochemical pathway shift from a $2e^-$ to a more efficient $4e^-$ process. (a and b) Galvanostatic intermittent titration technique (GITT) results for (a) discharge and (b) charge reveal a thermodynamic shift to a different reaction under hydro-photo system. (c and d) *In situ* differential electrochemical mass spectrometry (DEMS) quantifies the electron-to-oxygen ratio ($e^-/O_2$) during (c) discharge and (d) charge. (e) The total amount of $O_2$ consumed during discharge and evolved during charge is compared for both systems. (f) Charge and discharge profiles at 0.1 mA $cm^{-2}$. (g and h) FTIR spectra (g) and Raman spectra (h) of the electrode surface after charging. The demonstrated $4e^-$ pathway enhances $O_2$ utilization and improves reaction reversibility by suppressing parasitic side reactions.

process improves the utilization of oxygen and reduces the side reactions brought about by discharge products with oxidative properties. Moreover, there are no reduction or evolution of $H_2$ under hydro-photo, indicating that the dense LATP solid-state electrolyte effectively isolates the lithium anode from direct contact with water vapor, inherently preventing its corrosion.

The combination of sustained photocatalysis and an efficient $4e^-$ pathway translates into superior overall electrochemical performance. The P-SSLOB under hydro-photo exhibits a high discharge potential of 3.1 V and a low charge potential of 3.4 V, resulting in a small voltage hysteresis of only 0.3 V and a high round-trip efficiency of 91.2% (Fig. 4f). This is a dramatic improvement over the system under photo (2.7 V and 3.8 V), which suffers from a high potential gap of 1.1 V and a low round-trip efficiency (73.12%). The excellent reversibility of the system under hydro-photo was further confirmed by post-cycling characterization. After charging, the LiOH product decomposed completely, restoring the pristine cathode, whereas the $Li_2O_2$ under photo showed incomplete decomposition and particle agglomeration, leading to interfacial passivation (Fig. 4g and h, Fig. S16, 17).

### 3.4 Superior electrochemical performance and reversibility

The enhanced reversibility of the hydro-adapted P-SSLOB is also reflected in the EIS data. Under photo in Fig. 5a, the impedance significantly increases to 1200 Ω after discharging due to the insulating properties of $Li_2O_2$, and the impedance cannot return to the initial state after charging (only return to 700 Ω) due to the inability of the products to completely decompose leading to the passivation of the electrode surface. In contrast, the after-discharge impedance under hydro-photo (570 Ω) is much smaller than the discharge impedance under photo, which shows that the high ionic conductivity of the product makes the interfacial charge transfer kinetics under hydro-photo still superior (Fig. 5b). Its impedance after charging is almost the same as that before discharging, demonstrating the excellent reversibility of the charging and discharging process under hydro-photo.

The hydro-adapted P-SSLOB also demonstrates excellent rate capability (Fig. 5c) and outstanding cycling stability (Fig. 5d). It maintains a high discharge voltage of ~2.6 V even at a high current density of 0.5 mA $cm^{-2}$, which is much better than that of the cell under photo (~2.2 V). And the charging voltage (3.42

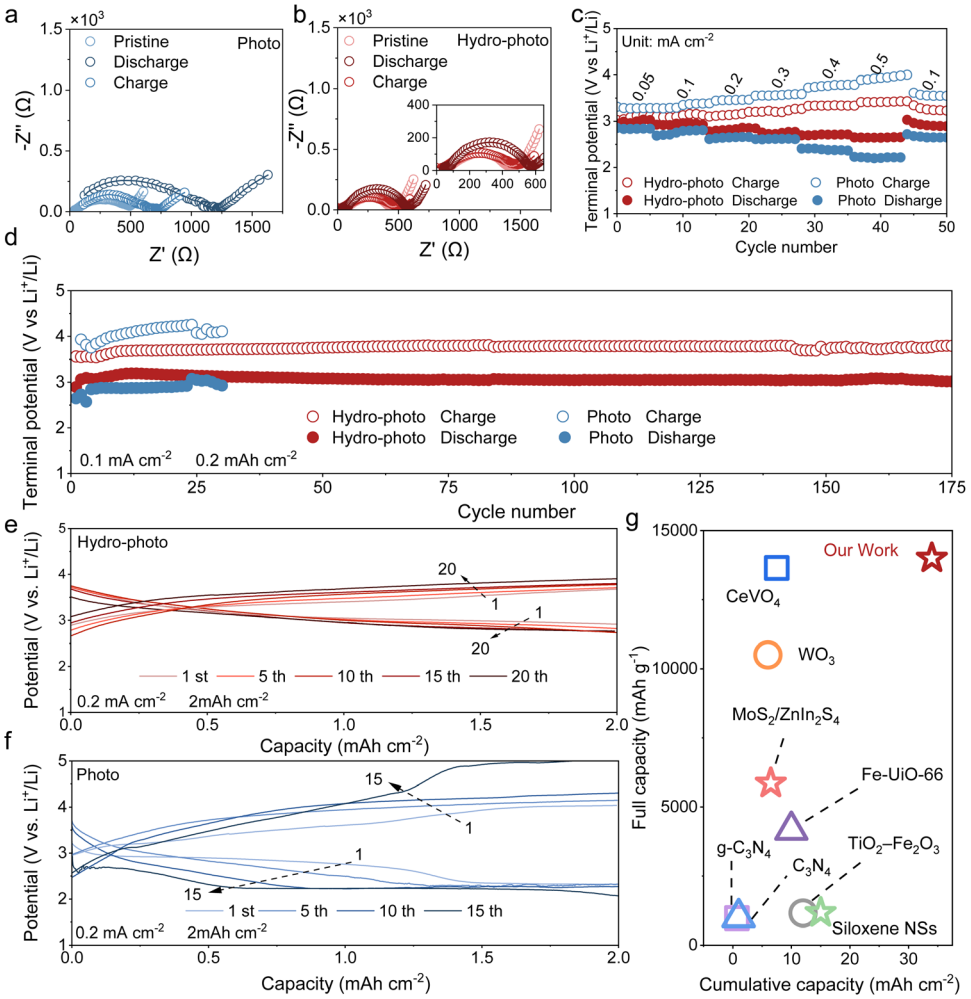


Fig. 5 Electrochemical performance and reversibility of the hydro-adapted P-SSLOB. (a and b) EIS spectra of the discharge and charge processes under (a) photo and (b) hydro-photo, respectively. (c) Discharge and charge voltage variation at different current densities. (d) Long-term cycling performance exhibits outstanding stability for over 170 cycles at a fixed capacity of 0.2 mA h $cm^{-2}$. (e and f) cycling performance at a fixed capacity of 2 mA h $cm^{-2}$ under (e) photo and (f) hydro-photo, respectively. (g) A benchmark chart compares the cumulative capacity of this work against previously reported state-of-the-art P-SSLOBs. Our hydro-adapted P-SSLOB outperforms the conventional system under photo and surpasses the performance of previously reported benchmarks across key metrics: voltage efficiency, rate capability, and long-term cycling stability.

V) and overpotential (0.82 V) of the cells under hydro-photo are much lower than those under photo (3.93 V and 1.73 V, respectively). Most impressively, the P-SSLOBs under hydro-photo demonstrated outstanding cycling stability, maintaining a high-potential discharge for over 170 cycles with a fixed capacity of 0.2 mAh $cm^{-2}$ at 0.1 mA $cm^{-2}$ (Fig. 5d). The characterization *via* SEM and XRD after cycling (Fig. S21) revealed no signs of corrosion, pulverization, or abnormal dendritic growth on the lithium anode, demonstrating its morphological stability. The cell under hydro-photo exhibited stable cycling performance at high-potential plateau with a fixed capacity of 2 mAh $cm^{-2}$ at 0.2 mA $cm^{-2}$ (Fig. 5e). However, two plateaus appeared in the first cycle of discharge due to the opaque $Li_2O_2$ under photo and the high-potential capacity gradually decreased with the number of cycles (Fig. 5f). This ultra-stable performance is attributed to the complete and reversible decomposition of LiOH during charge, enabled by its high ionic conductivity and the sustained photocatalytic activity, which prevents the interfacial passivation observed in the system under photo (Fig. S16). A comprehensive comparison highlights that the cumulative and the total capacities achieved in our work surpass most previously reported levels for P-SSLOBs (Fig. 5g and Table S3).[15,16,20–24,42–44]

## 4 Conclusions

In summary, we have shown that catalyst photo-shielding by opaque discharge products is a primary failure mechanism in P-SSLOBs. Our hydro-photo-synergy strategy, which transforms $Li_2O_2$ to transparent LiOH *in situ*, completely overcomes this limitation. This approach simultaneously sustains photocatalysis and unlocks a more efficient four-electron chemistry, leading to a dramatic enhancement in capacity, efficiency, and cyclability. This work provides a clear and scalable path to

realizing the promise of high-energy photo-assisted batteries. Furthermore, by demonstrating that controlled amounts of water are not detrimental but in fact beneficial, our findings challenge conventional battery design wisdom and align the technology more closely with practical applications, as operation in ambient air naturally provides the necessary humidity. This work offers new insights into other photocatalytic/photoelectrochemical systems (*e.g.*, water splitting, $CO_2$ reduction, and photoelectrochemical sensors) that suffer from performance degradation due to product deposition.

## Author contributions

Sijia Chi: writing – original draft, investigation, data curation. Zhenshen Li: investigation, methodology. Xunjie Yin: methodology, formal analysis. Shuoyi Chen: software, resources. Xuerui Yi: supervision, resources. Yiqiao Wang: supervision, resources. Yong Guo: investigation, methodology. Fangbing Li: resources, formal analysis. Shichao Wu: writing – review & editing, funding acquisition. Quan-Hong Yang: writing – review & editing, conceptualization.

## Conflicts of interest

There are no conflicts to declare.

## Data availability

The data that support the findings of this study are available in the supplementary information (SI) of this article. Supplementary information: XRD, SEM, BET, UV-vis and supporting data for this article. See DOI: https://doi.org/10.1039/d5sc08815a.

## Acknowledgements

The authors appreciate the support from the National Natural Science Foundation of China (No. 52272231), the National Key Research and Development Program of China (No. 2021YFF0500600), the Natural Science Foundation of Tianjin Municipality (No. 24JCZDJC00400), the Haihe Laboratory of Sustainable Chemical Transformations, and the Fundamental Research Funds for the Central Universities.

## References

1 X. Chi, M. Li, J. Di, P. Bai, L. Song, X. Wang, F. Li, S. Liang, J. Xu and J. Yu, *Nature*, 2021, **592**, 551–557.
2 F. Wu, J. Maier and Y. Yu, *Chem. Soc. Rev.*, 2020, **49**, 1569–1614.
3 Z. Wang, H. Yang, S. Li, H. Tong, W. Xu, Y. Zhao and L. Li, *Energymater*, 2024, **4**(400080).
4 C. Xia, C. Y. Kwok and L. F. Nazar, *Science*, 2018, **361**, 777–781.
5 Y. Wang, C. J. Zanelotti, X. Wang, R. Kerr, L. Jin, W. H. Kan, T. J. Dingemans, M. Forsyth and L. A. Madsen, *Nat. Mater.*, 2021, **20**, 1255–1263.
6 X. Sun, Y. Song, Q. Liu, X. Zhang, H. An, N. Sun, Y. Shi, C. Fu, H. Huo, Y. Xie, Y. Tong, F. Kong and J. Wang, *Sci. Adv.*, 2022, **8**, eabq6261.
7 Q. Zhang, Y. Li, E. T. Poh, Z. Xing, M. Zhang, M. Wang, Z. Sun, J. Pan, S. V. C. Vummaleti, J. Zhang and W. Chen, *Adv. Energy Mater.*, 2023, **13**, 2301748.
8 Y. Guo, S. Wu, Y.-B. He, F. Kang, L. Chen, H. Li and Q.-H. Yang, *eScience*, 2022, **2**, 138–163.
9 Y.-Z. Wang, Z.-L. Jiang, B. Wen, Y.-H. Huang and F.-J. Li, *J. Electrochem.*, 2024, **30**(8), 2314004.
10 J.-H. Wang, S. Li, Y. Chen, L.-Z. Dong, M. Liu, J.-W. Shi, S.-L. Li and Y.-Q. Lan, *Adv. Funct. Mater.*, 2022, **32**, 2210259.
11 D. Du, Z. Zhu, K.-Y. Chan, F. Li and J. Chen, *Chem. Soc. Rev.*, 2022, **51**, 1846–1860.
12 Y. Zhou, K. Yin, Q. Gu, L. Tao, Y. Li, H. Tan, J. Zhou, W. Zhang, H. Li and S. Guo, *Angew. Chem., Int. Ed.*, 2021, **60**, 26592–26598.
13 Y. Cheng, Y. Wang, B. Chen, X. Han, F. He, C. He, W. Hu, G. Zhou and N. Zhao, *Adv. Mater.*, 2024, **36**, 2410704.
14 Y. Liu, N. Li, S. Wu, K. Liao, K. Zhu, J. Yi and H. Zhou, *Energy Environ. Sci.*, 2015, **8**, 2664–2667.
15 Z. Zhu, X. Shi, G. Fan, F. Li and J. Chen, *Angew. Chem., Int. Ed.*, 2019, **58**, 19021–19026.
16 M. Li, X. Wang, F. Li, L. Zheng, J. Xu and J. Yu, *Adv. Mater.*, 2020, **32**, 1907098.
17 H. Yu, D. Liu, Z. Fu, S. Wang, X. Zuo, X. Feng and Y. Zhang, *Angew. Chem., Int. Ed.*, 2024, **63**, e202401272.
18 Z. Zhang, K. Xiang, H. Wang, X. Li, J. Zou, G. Liang and J. Jiang, *SusMat*, 2024, **4**, e229.
19 L. Ren, M. Zheng, F. Kong, Z. Yu, N. Sun, M. Li, Q. Liu, Y. Song, J. Dong, J. Qiao, N. Xu, J. Wang, S. Lou, Z. Jiang and J. Wang, *Angew. Chem., Int. Ed.*, 2024, **136**, e202319529.
20 Y. Liu, N. Li, K. Liao, Q. Li, M. Ishida and H. Zhou, *J. Mater. Chem. A*, 2016, **4**, 12411–12415.
21 Y. Yang, X. Hu, G. Wang, J. Han, Q. Zhang, W. Liu, Z. Xie and Z. Zhou, *Adv. Funct. Mater.*, 2024, **34**, 2315354.
22 L. Ren, M. Zheng, F. Kong, Z. Yu, N. Sun, M. Li, Q. Liu, Y. Song, J. Dong, J. Qiao, N. Xu, J. Wang, S. Lou, Z. Jiang and J. Wang, *Angew. Chem., Int. Ed.*, 2024, **136**, e202319529.
23 H. Gong, T. Wang, K. Chang, P. Li, L. Liu, X. Yu, B. Gao, H. Xue, R. Ma, J. He and J. Ye, *Carbon Energy*, 2022, **4**, 1169–1181.
24 M. Wang, J. Chen, Z. Tian, W. Dai, B. Cui, X. Cui, D. Wang, Y. Xiao, X. Lian, C. Jiang, H. Yang, Y. Wang, Z. Sun, Y. Ding, Y.-Y. Sun, J. Zhang and W. Chen, *Energy Environ. Sci.*, 2023, **16**, 523–534.
25 R. Li, F. Zhang, D. Wang, J. Yang, M. Li, J. Zhu, X. Zhou, H. Han and C. Li, *Nat. Commun.*, 2013, **4**, 1432.
26 F. Matter and M. Niederberger, *Adv. Sci.*, 2022, **9**, 2105363.
27 H. Gong, H. Xue, B. Gao, Y. Li, X. Yu, X. Fan, S. Zhang, T. Wang and J. He, *Chem. Commun.*, 2020, **56**, 13642–13645.
28 Y. Wang, S. Pan, H. Li, D. Li, Y. Guo, S. Chi, C. Geng, S. Wu and Q.-H. Yang, *EES. Catal.*, 2023, **1**, 213.
29 L.-N. Song, L.-J. Zheng, X.-X. Wang, D.-C. Kong, Y.-F. Wang, Y. Wang, J.-Y. Wu, Y. Sun and J.-J. Xu, *J. Am. Chem. Soc.*, 2024, **146**, 1305–1317.

30 V. Viswanathan, K. S. Thygesen, J. S. Hummelshøj, J. K. Nørskov, G. Girishkumar, B. D. McCloskey and A. C. Luntz, *J. Chem. Phys.*, 2011, **135**, 214704.
31 M. D. Radin and D. J. Siegel, *Energy Environ. Sci.*, 2013, **6**, 2370–2379.
32 F. M. Pesci, A. Bertei, R. H. Brugge, S. P. Emge, A. K. O. Hekselman, L. E. Marbella, C. P. Grey and A. Aguadero, *ACS Appl. Mater. Interfaces*, 2020, **12**, 32806–32816.
33 Y. Lu, C.-Z. Zhao, J.-K. Hu, S. Sun, H. Yuan, Z.-H. Fu, X. Chen, J.-Q. Huang, M. Ouyang and Q. Zhang, *Sci. Adv.*, 2022, **8**, eadd0510.
34 M. R. Busche, M. Weiss, T. Leichtweiss, C. Fiedler, T. Drossel, M. Geiss, A. Kronenberger, D. A. Weber and J. Janek, *Adv. Mater. Inter.*, 2020, **7**, 2000380.
35 X.-S. Yang, Y. Meng and D. Xiao, *J. Mater. Chem. A*, 2022, **10**, 24628–24638.
36 G. Tian, H. Xu, X. Wang, X. Wen, T. Zeng, S. Liu, F. Fan, W. Xiang and C. Shu, *Nano Energy*, 2023, **117**, 108863.
37 B. Hwang, M.-C. Sung, S. Jung, M. S. Kim and D.-W. Kim, *SusMat*, 2025, **5**, e70020.
38 D. Guo, J. Wu, Z. Liu, X. Liu, Z. Xu, Z. Gu, X. Yao and X. Xin, *ACS Appl. Energy Mater.*, 2024, **7**, 275–284.
39 M. M. Ottakam Thotiyl, S. A. Freunberger, Z. Peng and P. G. Bruce, *J. Am. Chem. Soc.*, 2013, **135**, 494–500.
40 B. D. McCloskey, A. Speidel, R. Scheffler, D. C. Miller, V. Viswanathan, J. S. Hummelshøj, J. K. Nørskov and A. C. Luntz, *J. Phys. Chem. Lett.*, 2012, **3**, 997–1001.
41 Y. Qiao and S. Ye, *J. Phys. Chem. C*, 2016, **120**, 8033–8047.
42 D. Li, X. Lang, Y. Guo, Y. Wang, Y. Wang, H. Shi, S. Wu, W. Wang and Q.-H. Yang, *Nano Energy*, 2021, **85**, 105966.
43 Z. Zhu, Q. Lv, Y. Ni, S. Gao, J. Geng, J. Liang and F. Li, *Angew. Chem., Int. Ed.*, 2022, **61**, e202116699.
44 C. Jia, F. Zhang, L. She, Q. Li, X. He, J. Sun, Z. Lei and Z.-H. Liu, *Angew. Chem., Int. Ed.*, 2021, **133**, 11357–11361.